PAPER Nr.: 35

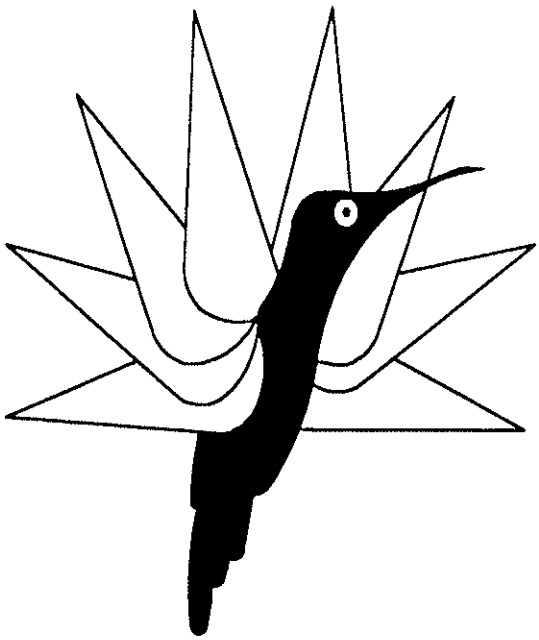

Flexibility Enhancement of Euler Codes for Rotor Flows by Chimera Techniques

by

K. Pahlke and J. Raddatz

DLR, Institute of Design Aerodynamics
Lilienthalplatz 7, 38108 Braunschweig, F.R. Germany

TWENTIETH EUROPEAN ROTORCRAFT FORUM
OCTOBER 4 - 7, 1994 AMSTERDAM

Printed by the Technical Highschool Haarlem

TWENTIETH EUROPEAN ROTORCRAFT FORUM
AMSTERDAM, The Netherlands, October 4th - 7th, 1994

Paper No. 35

Flexibility Enhancement of Euler Codes for Rotor Flows by Chimera Techniques

DLR, Institute of Design Aerodynamics
Lilienthalplatz 7, 38108 Braunschweig, F.R. Germany
K. Pahlke and J. Raddatz

Summary:

The implementation of a chimera grid scheme based on the Euler equations for steady and unsteady flows is described. At the chimera boundaries linear interpolation of flow quantities is used based on triangles or tetrahedrons.

Conventional and chimera results are compared for steady and unsteady transonic 2D flows showing good agreement.

The comparison of the solutions for a hovering rotor using a conventional single block, a conventional 2 block and a chimera grid shows that a first order boundary treatment at inner boundaries is not sufficient. The chimera solution reproduced all flow features but the vortex is captured less sharply.

List of symbols:

c	chord
c_p	pressure coefficient 2D: $c_p = \frac{p - p_\infty}{\frac{1}{2}\rho_\infty (\vec{q}_\infty)^2}$ 3D: $c_p = \frac{p - p_\infty}{\frac{1}{2}\rho_\infty (\omega \cdot r)^2}$
E	total specific energy
F	flux tensor
$\vec{G}$	vector of source terms
H	total specific enthalpy
k	reduced frequency $k = \frac{\omega \cdot c}{2 \cdot \lvert\vec{q}_\infty\rvert}$
$\vec{n}$	unit outward to ∂V
p	pressure
$\vec{q}$	velocity vector
$\vec{q}_b$	vector of the velocity of a control volume boundary
r	radial position of a rotor section
$\vec{r}$	$= (x, y, z)^T$ coordinate vector
R	rotor radius
dS	surface element
t	time
u, v, w	Cartesian velocity components
V	control volume
dV	volume element
∂V	boundary of V
$\vec{W}$	vector of conservative variables
x, y, z	Cartesian coordinates
γ	ratio of specific heats
θ	pitching angle
ρ	density
ψ	azimuth
ω	angular velocity ($\omega = d\psi/dt$)

1. Introduction

Most of the current methods for the flowfield prediction of rotors in forward flight are coupled with integral wake models to introduce the influence of the vortex wake.These methods range from relatively simple boundary integral methods up to more sophisticated computational fluid dynamics (CFD) codes ((1), (2),

(3)) obtaining results of high accuracy for many cases, but always dominated by the wake model (4). Using a prescribed wake model, the wake has to be specialized for each blade shape, making it difficult to treat blades with arbitrary twist, taper or planform. Also some potential flow methods have been coupled with a free-wake approach, in which the wake is allowed to convect freely with the flow without constraining its trajectory (5). These methods are restricted in the treatment of compressibility and transonic effects, which are features of the flow around advanced high speed helicopter rotors.

Since the rotor and its wake constitute a tightly coupled system it is natural to solve the flow around the blade and the wake with a unified flow method. For hover cases several unified blade/wake computations have been carried out using full potential (velocity decomposition approach, (6), (7)), Euler (8) or Navier-Stokes methods (9).

It is much more difficult to use a unified flow method for lifting forward flight cases because the relative motion of the rotor blades prevents the use of a rigid grid around the complete rotor. There are two different ways to perform full Euler/Navier-Stokes simulations for a rotor consisting of several blades in relative motion. The first one is to use a deforming grid for the whole rotor to enable the full movement of each blade. This approach has the disadvantage that a new 3D grid has to be generated at each blade position. Subsequently it is necessary to recalculate the metric terms as well as the grid velocities for each variation of the grid. The second way is to generate several rigid grids to discretize the whole rotor, one grid around each blade and an overlapping background grid. Using this approach, known as chimera technique (10) in the literature, there is no need to generate grids or calculate metric terms during the run of the flow solver. Furthermore, a chimera scheme is very attractive for the computation of the flow around rotor and fuselage or a complete helicopter. Disadvantages are the additional computational effort for interpolation routines and the errors which are introduced by the interpolation at the inner boundaries.

Considering the above arguments it was decided to investigate the suitability of a chimera scheme which is based on the Euler equations for rotor flows.

The objective of this paper is the comparison of accuracy and efficiency of steady (2D and 3D) and time-accurate (2D) Euler computations with and without overlapping grids.

2. Governing equations

A general rigid body motion can be described as a translatory motion with the translatory velocity $\vec{q}_0$ and a rotation of the rigid body around 1 (2D) or 3 axis (3D). Figure 1 illustrates the relation between the inertial (x, y) and the moving (x_r, y_r) coordinate system for the 2D case. Let $\vec{q}_r = [u_r, v_r]^T$ be the velocity vector referred to the (x_r, y_r) system which does not contain the rotational velocities. Then

$$\vec{q}_r = T^{-1} \cdot \vec{q} \text{ with } T = \begin{bmatrix} \cos\alpha & \sin\alpha \\ -\sin\alpha & \cos\alpha \end{bmatrix}.$$

By this choice of $\vec{q}_r$ the absolute values of $\vec{q}_r$ and $\vec{q}$ are the same and $\vec{q}_r$ can be calculated by $\vec{q}$ and α, independently of x and y. This is especially important for the formulation of the farfield boundary condition.

The unsteady Euler equations have been transformed into the moving coordinate system (x_r, y_r). For brevity only the equations for the 2D case are given. The transformed equations read:

$$\frac{d}{dt}\int_{V_r} \vec{W}_r\, dV_r + \int_{\partial V_r} F_r' \cdot \vec{n}_r\, dS_r - \int_{\partial V_r} F_r'' \cdot \vec{n}_r\, dS_r + \omega \int_{V_r} \vec{G}_r\, dV_r = 0 \qquad (1)$$

with

$$\vec{W}_r = \begin{bmatrix} \rho \\ \rho u_r \\ \rho v_r \\ \rho E_r \end{bmatrix}; F_r' = \begin{bmatrix} \rho \vec{q}_r \\ \rho u_r \vec{q}_r + p\vec{i}_{x_r} \\ \rho v_r \vec{q}_r + p\vec{i}_{y_r} \\ \rho H_r \vec{q}_r \end{bmatrix};$$

$$F_r'' = \begin{bmatrix} \rho \vec{q}_{b,r} \\ \rho u_r \vec{q}_{b,r} \\ \rho v_r \vec{q}_{b,r} \\ \rho E_r \vec{q}_{b,r} \end{bmatrix}; \vec{G}_r = \begin{bmatrix} 0 \\ \rho v_r \\ -\rho u_r \\ 0 \end{bmatrix}.$$

This system of equations is closed by

$$p = (\gamma - 1)\,\rho\left(E_r - \frac{u_r^2 + v_r^2}{2}\right) \text{ and}$$

$$H_r = E_r + \frac{p}{\rho}.$$

Analogous relations hold in three dimensions with a third momentum equation and a source term containing additional angles and angular velocities accounting for the additional degrees of freedom of a 3D rigid body.

3. Numerical Aspects

3.1 Spatial and Temporal Discretization

The discretization of space and time is separated following the method of lines (Jameson et al. (11) using a cell-centered finite volume formulation for the spatial discretization. The flow quantities $\vec{w}_r$ and the source term $\vec{c}_r$ are taken to be volume averaged and are located at the center of the grid cell. The finite volume discretization reduces to a second-order central difference scheme on a Cartesian grid with constant grid sizes. If an arbitrary non uniform grid is used, the accuracy depends on the smoothness of the grid. In order to avoid spurious oscillations a blend of first and third order dissipative terms is introduced.

An explicit Runge-Kutta time stepping scheme is used with an evaluation of the dissipatve fluxes at the first two stages (11). In order to accelerate the convergence to steady state local time steps, enthalpy damping and implicit residual averaging have been implemented. The implicit residual averaging has been adapted to time-accurate computations (12).

3.2 Boundary Conditions

A zero flux condition is used at the surface of solid bodies. The far field boundary is treated following the concept of Characteristic Variables for non-reflecting boundary conditions (13). Auxiliary cells are used to store the neighbour flow values in order to match the solution across inner cuts. In order to have second order spatial accuracy at inner cuts it is necessary to use two layers of auxiliary cells. Up to now only the 2D version uses two layers. The 3D version still uses only one layer of auxiliary cells which reduces the spatial accuracy to first order at cuts.

3.3 Chimera Algorithm

The basic idea of the chimera scheme is to generate body conforming grids (so called child grids) around different bodies independently and to embed these grids into a background grid (so called father grid). There is no need for common boundaries between the grids, but rather an overlap region is required between a child grid and the father grid to provide the means for matching the solutions across the boundary interfaces. The present chimera scheme has been implemented according to references (10) and (14). Figure 2 shows a child grid embedded into a father grid

for a NACA 0012 airfoil. Since the airfoil in the child grid is an impermeable body with no flow through it, the points of the father grid that fall within the rotor blade are excluded or blanked from the flow field solution. These blanked out points in the father grid form a "hole" in the father grid. The cells of the father grid in Figure 2 are shaded grey except for the hole cells. The boundary of this hole is the first of two interface boundaries, that arise because of the use of the chimera scheme. Data for this hole boundary is supplied from the solution contained on the child grid. The outer boundary of the child grid forms the second interface. Flow values for the dummy layer at this outer boundary are provided from the father grid. In this implementation only flow values are exchanged at the chimera boundaries, which simplifies the algorithm, but yields a non-conservative scheme. As it is shown in (15) this can result in inaccurate solutions for supersonic or hypersonic flows. This deficiency can be corrected by a chimera boundary treatment with conservative flux interpolation. On the other hand several publications show that non-conservative chimera schemes produce accurate solutions for sub- or transonic flows, when it is assured that no shocks cross the chimera boundaries.

In order to provide the flow values at the grid interfaces it is necessary to use interpolation formulae. Different approaches have been published. Higher order interpolation has the advantage of higher spatial accuracy, but unfortunately it may introduce instabilities into the schemes. Therefore bilinear (2D) or trilinear (3D) interpolation using the node points of quadrilateral (2D) cells or hexahedrons (3D) is used in most implementations. This approach is computationally very efficient but it does not ensure that the interpolated point lies within the cell (especially for skewed cells). For these reasons a linear interpolation based on triangles (2D) or tetrahedrons (3D) was chosen for the present work which consumes more cpu-time but guarantees that all interpolation coefficients are positive and less or equal 1. Hence it is necessary to find for each boundary point the triangle or tetrahedron which contains the boundary point. This search takes advantage of the fact that structured grids are used (14). For steady cases the search algorithm is run only once.

The time stepping scheme is changed with regard to a special treatment of the hole points. The algorithm is modified such that the flow values for the hole in the father grid are not updated by the Runge-Kutta scheme nor the implicit residual smoothing nor the enthalpy damping.

4. Results

4.1 Steady 2D Cases

NACA 0012 Airfoil

The first steady 2D test case is the standard case of the flow around a NACA 0012 airfoil with $M_\infty = 0.8$ and $\alpha = 1.25\,^\circ$. Three conventional O-type grids have been used with 80x16, 160x32 and 320x64 cells. The medium and the coarse grid have been generated by skipping every other point of the fine grid or the medium grid respectively. The far field distance is 40 chords. Figure 3 shows the coarse, the medium and the fine grid in the vicinity of the airfoil. For the generation of the chimera father grids Cartesian H-type grids were generated with 48x48, 64x64 and 128x128 cells. The grid cells are clustered in the region of the child grid and stretched at the far field. The clustered region of the 48x48 grid can be seen in Figure 2. The medium grid was obtained by skipping every other point from the fine grid. For accurate results it is necessary that the neighbouring cells at chimera boundaries have approximately the same size and aspect ratio. Therefore it was not possible to obtain the coarse father grid in the usual way out of the medium grid. In order to have a fair comparison the child grids were generated out of the

conventional grids by skipping the second half of the grid cells in normal direction. This results in O-type child grids with 80x8, 160x16 and 320x32 cells (see Figure 3). Figure 4 presents the pressure distributions for the coarse, the medium and the fine grid. The results of the chimera calculation agree well with the conventional O-grid results.

Karmann-Trefftz-Airfoil

The second steady test case is the Karmann-Trefftz airfoil with a $30°$ deflected flap (16). Two O-type grids were generated independently around the main airfoil and the flap. The grid around the main airfoil is the father grid and the flap grid is the child grid (see Figure 5). The pressure distribution for this test case is shown in Figure 6. For the chimera computation $M_\infty = 0.15$ was used. The analytical solution assumes incompressible flow ($M_\infty = 0.0$). The results of the chimera computation and the analytical solution are in excellent agreement. This test case illustrates how the chimera technique can simplify the grid generation task for a complex configuration.

4.2 Unsteady 2D Case

The unsteady 2D test case is the flow around a NACA 0012 airfoil oscillating around its quarter point (AGARD Aeroelastic Configuration CT5). This test case is the exact 2D analogy to a rotor in forward flight. The same grids as in section 4.1 are used. The time convergence was checked by running three computations, 1000, 2000 and 4000 iterations per period. A comparison of the momentum as a function of angle of attack showed that 2000 iterations per period produce a fully time converged solution. Figures 7 and 8 show a comparison of instantaneous pressure distributions with and without chimera technique for the coarse and the medium grids and the experiment (17). The agreement between the chimera and the conventional solution on the coarse grids is good. For the medium grids the cp-curves of the two computations cannot be distinguished demonstrating the reduction of the interpolation error due to the grid refinement. The integral values in Figure 9 for the third period show a good agreement between a coarse one block calculation and a calculation on the coarse chimera grid system. The computations on the medium grids show almost identical results for the conventional and the chimera grid system (see Figure 10).

4.3 Steady 3D Case

The steady 3D test case chosen is one of the well known hover test cases of Caradonna and Tung (18).

Two body conforming, single block, computational grids were constructed, using a grid generator based on an elliptic 3D solver (for details see (19)). The first grid has a blade pitch of $0°$ and the second a blade pitch of $8°$. Because of the cylindrical nature of the flow of a hovering rotor an O-H topology was chosen with the wraparound O in chordwise direction and the H-type in spanwise direction.

Due to the symmetry of the flow only half of the rotor plane containing one blade has to be regarded. The other blade is taken into account by periodicity conditions in the blade azimuthal direction, which swaps the flow information at the front and back boundaries of the cylindrical mesh. On account of this grid topology it is obvious to generate grids with identical point distributions on the periodicity planes. Therefore, no interpolation of the flow quantities on the periodicity planes is required.

Figure 11 presents the shape of the grids in the rotor plane. The grids have 112 cells in the wraparound (along the chord) direction, 64 cells in the spanwise (radial) direction (40 cells

on the blade surface), and 40 cells in the normal direction. The grid is clustered near the leading and trailing edges and near the tip region to resolve the tip vortex.

In Euler-computations on grids containing the whole rotor disc the wake is part of the solution. Consequently no wake model is used for this hover case.

In order to have a fair comparison between the conventional and the chimera scheme three computations were carried out. The first computation used a conventional 1 block grid. For the second computation the grid is splitted in the blade normal direction into two conventional blocks. The third computation is run with the chimera scheme and uses the grid with $0°$ pitch angle as father grid and the inner part of this grid as child grid, which is rotated around the quarter line to give the pitch angle of $8°$. This procedure is of course not typical for overlapping grids but it was chosen to eliminate possible differences due to different grid shapes or different clustering. Figure 12 shows the father and the child grid in the rotor plane. An index plane at a cross section of $r/R = 0.50$ is plotted in Figure 13 presenting the father grid, the hole cells of the father grid and the child grid.

Figure 14 represents the surface grid of the rotor and compares computational results of a conventional single block, a conventional two block and a chimera two block solution with the experimental data. The agreement between the three computations is not as good as for the 2D cases. There are differences between the conventional single and two block computations. These differences, especially a shock position which is slightly further downstream at $r/R = 0.89$ and $r/R = 0.96$, are due to the first order boundary treatment at the inner block boundaries. The chimera two block computation uses the same boundary treatment at the outer boundaries of the child grid. In addition first order interpolation errors occur at the hole boundaries of the father grid and at the outer boundaries of the child grid which increases the differences between the conventional single block and the chimera computation. The comparison with the experimental values demonstrates that it is necessary to include viscous terms for a correct prediction of thrust.

In order to visualize the trailing vortices and the wake of a rotor the vorticity ($= |\vec{\nabla} \times \vec{q}|$) is plotted in a radial plane vertical to the rotor disc $20°$ azimuth behind the rotor blade. Figure 15 demonstrates the position of this plane in the rotor disc. The vorticity is plotted for the three computations in Figure 16. The small white gaps in the results for the 1 block and the 2 block calculations are due to the fact that a cell-centered scheme is used and therefore the position of the flow quantities at the end and the beginning of an inner cut is different. The $20°$ old tip vortex is represented at the end of the rotor disc by concentrated vorticity iso-lines. The vortex of the preceding blade has moved below the rotor disc and about 15% radius closer to the hub. Going from the single block to the 2 block and the chimera calculation the vortex is widened and is resolved less sharply. The results for the chimera calculation had to be reconstucted using cells of the father and the child grid. This can be recognized in a slight displacement of the vorticity iso-lines.

5. Conclusion

A chimera grid scheme based on the Euler equations has been implemented for steady 2D and 3D and unsteady 2D flows. At the chimera boundaries linear interpolation of flow quantities is used based on triangles or tetrahedrons which ensures that all interpolation coefficients are positive and less or equal 1.

For steady cases the chimera scheme consumes about 5% more cpu-time on a CRAY Y-MP computer per grid cell and time step com-

pared to the conventional scheme with the same number of blocks. For unsteady cases the cpu-time is increased by 50% per grid cell and time step in the present implementation. This high increase in cpu-time is due to the fact that the CRAY Y-MP is a vector computer with a relatively poor performance for algorithms with many scalar instructions like search algorithms. It is assumed that this overhead can be reduced to about 20-30% by optimizing the search algorithm.

The increase of the overall computation time for the chimera scheme per test case is dominated by the number of grid cells in the overlapping region resulting in chimera grids with about 20 - 80% more grid points than the comparable conventional grids. No effort has been spend to minimize the overlap region in the present work.

Conventional and chimera results have been compared for steady and unsteady transonic 2D flows showing very good agreement.

Solutions for a hovering rotor using a conventional single block, a conventional 2 block and a chimera grid were compared. It was shown that for high accuracy results a first order boundary treatment of the conventional boundaries is not sufficient. This problem can be solved by a second layer of auxiliary cells. The chimera solution reproduced all flow features but the vortex is captured less sharply. Since vortex dissipation is an important problem for rotor flows the boundary treatment at the chimera boundaries has to be improved. For the results shown in section 4.3 the cell sizes and the cell aspect ratios were almost exactly the same at the chimera boundaries. It has to be investigated whether this is necessary for forward flight applications during the whole blade movement.

The very promising 2D results give hope that accurate forward flight solutions using the chimera technique will be possible.

6. Bibliography

1) Johnson, F.:'A General Panel Method for the Analysis and Design of Arbitrary Con figurations in Incompressible Flow', NASA CR-3079.

2) Chang, I.-C. and Tung, C.:*'Numerical Solution of the Full Potential Equation for Rotors and Oblique Wings Using a New Wake Model'*, AIAA Paper 85-0268.

3) Sankar, L.N. and Tung, C.:*'Euler Calculations for Rotor Configurations in Unsteady Forward Flight'*, 42nd Annual Forum of the American Helicopter Society, Washington, D.C. June 2-4, 1986.

4) Pahlke, K.; Raddatz, J.:*'3D Euler Methods for Multibladed Rotors in Hover and Forward Flight'*, Nineteenth European Rotorcraft Forum, Paper C20, Cernobbio (Como), Italy, September 1993.

5) Zerle, L. and Wagner, S.:*'Development and Validation of a Vortex Lattice Method to Calculate the Flowfield of a Helicopter Rotor Including Free Wake Development'*, 18th European Rotorcraft Forum, Paper 72, Avignon, France, September 1992.

6) Steinhoff, J. S. and Ramachandran, K.: 'A Vortex Embedding Method for Free Wake Analysis of Helicopter Rotor Blades in Hover', 13th European Rotorcraft Forum, Paper 2-11, Arles, France,September1987.

7) Ramachandran, K.; Tung, C. and Caradonna, F.X.:'The Free Wake Prediction of Rotor Hover Performance Using a Vortex Embedding Method', AIAA 89-0638, AIAA 27th Aerospace Sciences Meeting, Reno, NV, Jan. 9-12, 1989.

8) Kroll, N.:*'Computation of the Flow Fields of Propellers and Hovering Rotors using Euler Equations'*, 12th European Rotorcraft Forum, Paper 28, Garmisch-Partenkirchen, Germany, September 1986.

9) Srinivasan, G.R. and McCroskey, W.J.:*'Navier-Stokes Calculations of Hovering Rotor Flowfields'*, Journal of Aircraft, Vol. 25, No.10, pp. 865-874, 1988.

10) Benek, J. A.; Buning, P. G.; Steger, J. L.*'A 3-D Chimera Grid Embedding Technique'*, AIAA 7th Computational Fluid Dynamics Conference, Cinicinatti, Ohio, July 15-17,1985.

11) Jameson, A.; Schmidt, W.; Turkel, E.:*'Numerical Solutions of the Euler Equations by Finite Volume Methods Using Runge-Kutta Time Stepping Schemes'*, AIAA-Paper 81-1259 (1981).

12) Pahlke, K.; Blazek, J.; Kirchner, A.*'Time-Accurate Euler Computations for Rotor Flows.'* Royal Aeronautical Society, 1993 European Forum, Recent Developments and Applications in Aeronautical CFD, Bristol, UK, 1.-3. September, 1993.

13) Kroll, N.*'Berechnung von Strömungsfeldern um Propeller und Rotoren im Schwebeflug durch die Lösung der Euler-Gleichungen'*,DLR-FB 89-37.

14) Dougherty, F.C.:*'Development of a Chimera Grid Scheme with Applications to Unsteady Problems'*, Stanford University, Ph. D. 1985, June 1985.

15) Pärt-Enander, E.; Sjögren, B.' *Conservative and Non-Conservative Interpolation between Overlapping Grids for Finite Volume Solutions of Hyperbolic Systems'*, Computers Fluids, Vol. 23, No. 3, pp. 551-574, Pergamon Press, 1994.

16) Williams, B. R.*'An exact Test Case for the Plane Potential Flow About Two Adjacent Lifting Aerofoils'*, Reports and Memoranda No. 3717, Ministry of Defence, London, UK, September 1971.

17) Landon, R. H. *NACA 0012. Oscillatory and Transient Pitching.* AGARD-R-702, Dataset 3, August 1982.

18) Caradonna, F.X. and Tung, C.: *'Experimental and Analytical Studies of a Model Helicopter Rotor in Hover'*, NASA-TM 81232, September 1981.

19) Findling, A.; Herrmann, U.*'Development of an efficient and robust solver for elliptic grid generation'*, Proceedings of the Third International Conference on Numerical Grid Generation in Computational Fluid Dynamics and Related Fields, Barcelona, Spain, 1991.

7. Figures

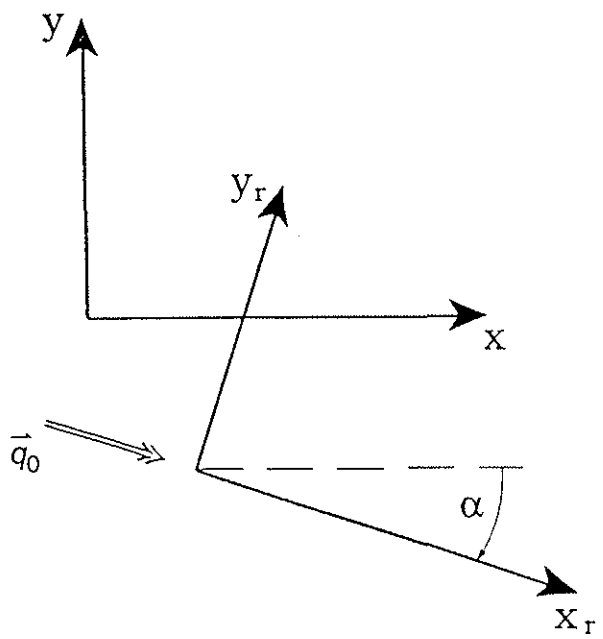

Figure 1: Inertial (x, y) and Moving (x_r, y_r) Coordinate System

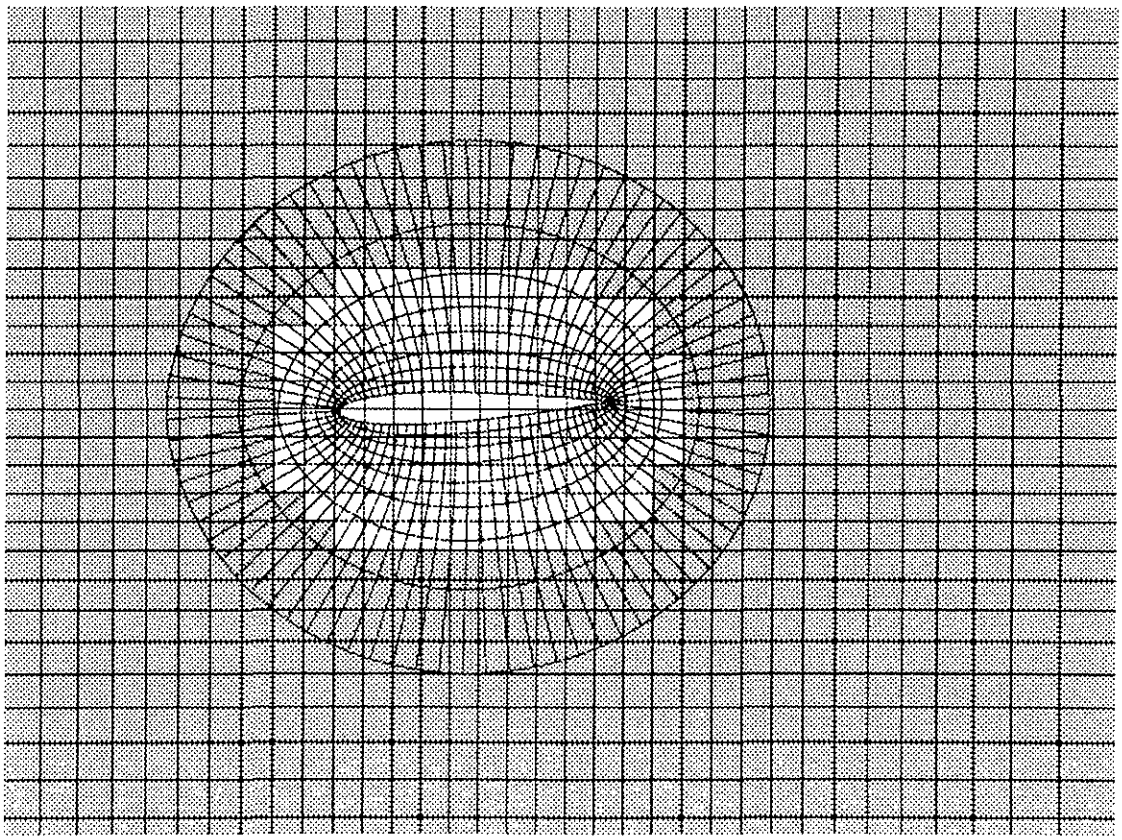

Father grid cells shaded grey except for the 'hole'

Figure 2: H-Type Father Grid and O-Type Child Grid

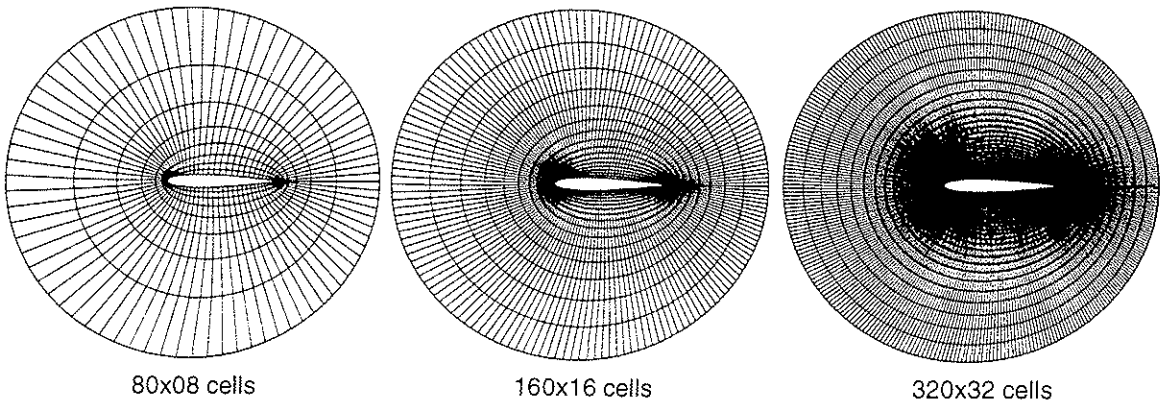

Figure 3: O-Type Grids around a NACA 0012 Airfoil

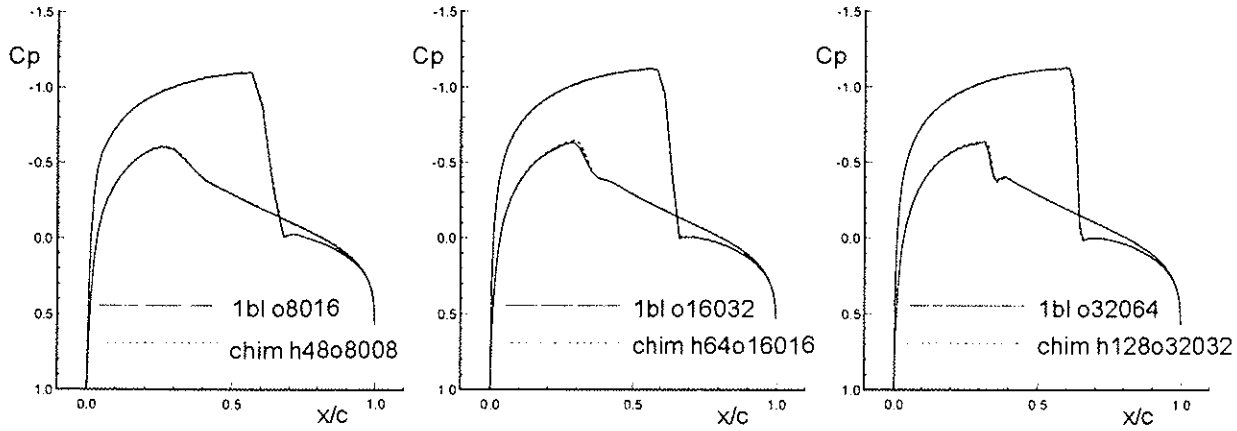

Figure 4: Grid Refinement Study for the Flow around a NACA 0012 Airfoil
$M_\infty = 0.8, \alpha = 1.25°$

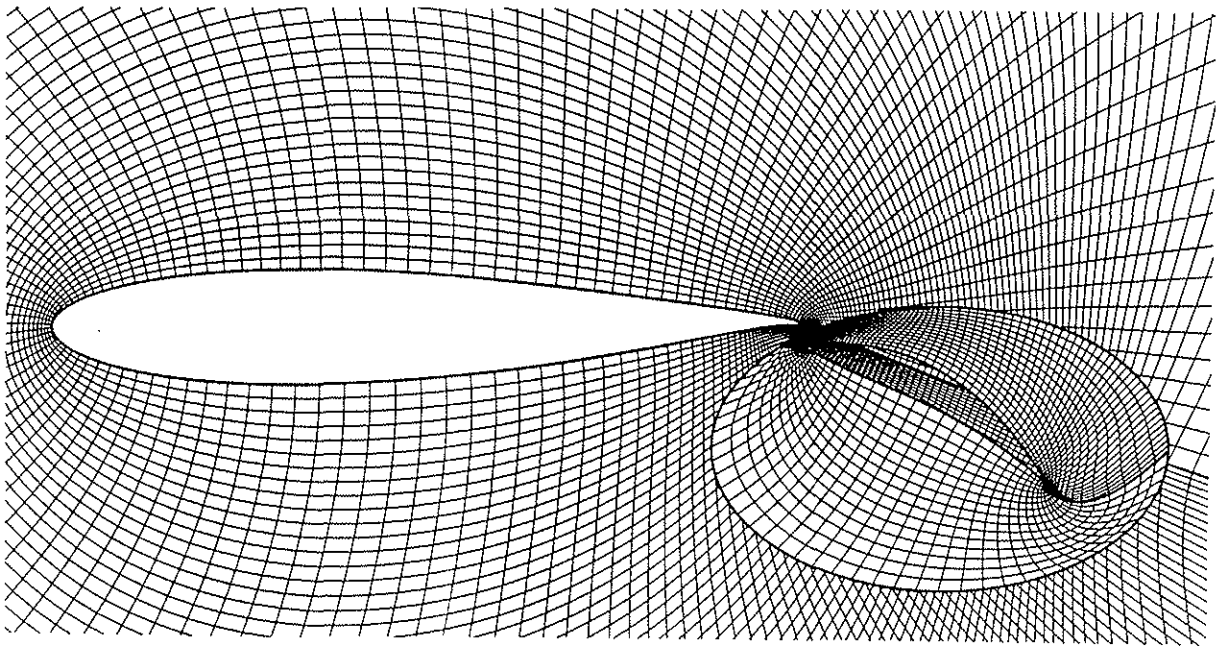

Figure 5: Overlapping Grids for the Karmann-Trefftz-Airfoil with a $30°$ deflected flap

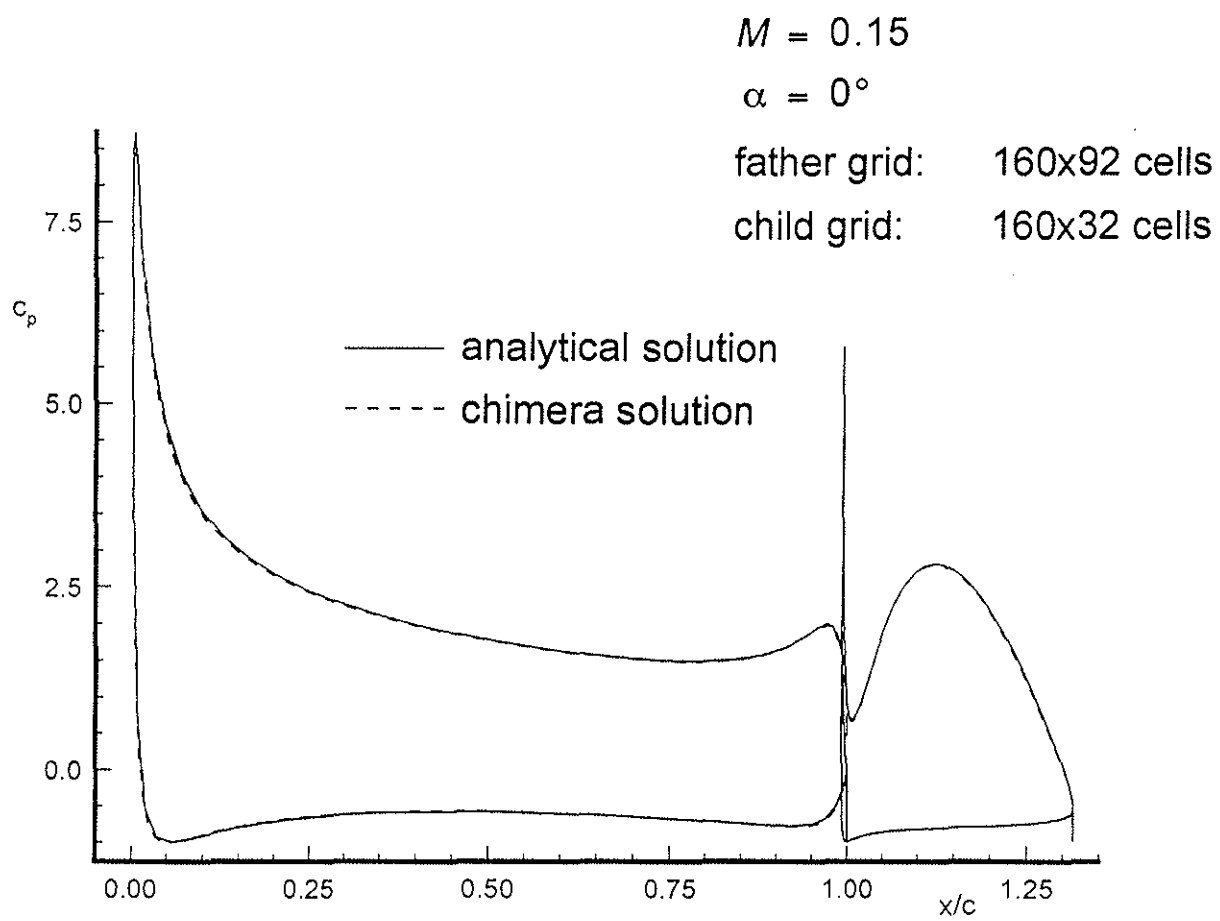

Figure 6: Pressure Distribution for the Karmann-Trefftz-Airfoil with a $30°$ deflected flap

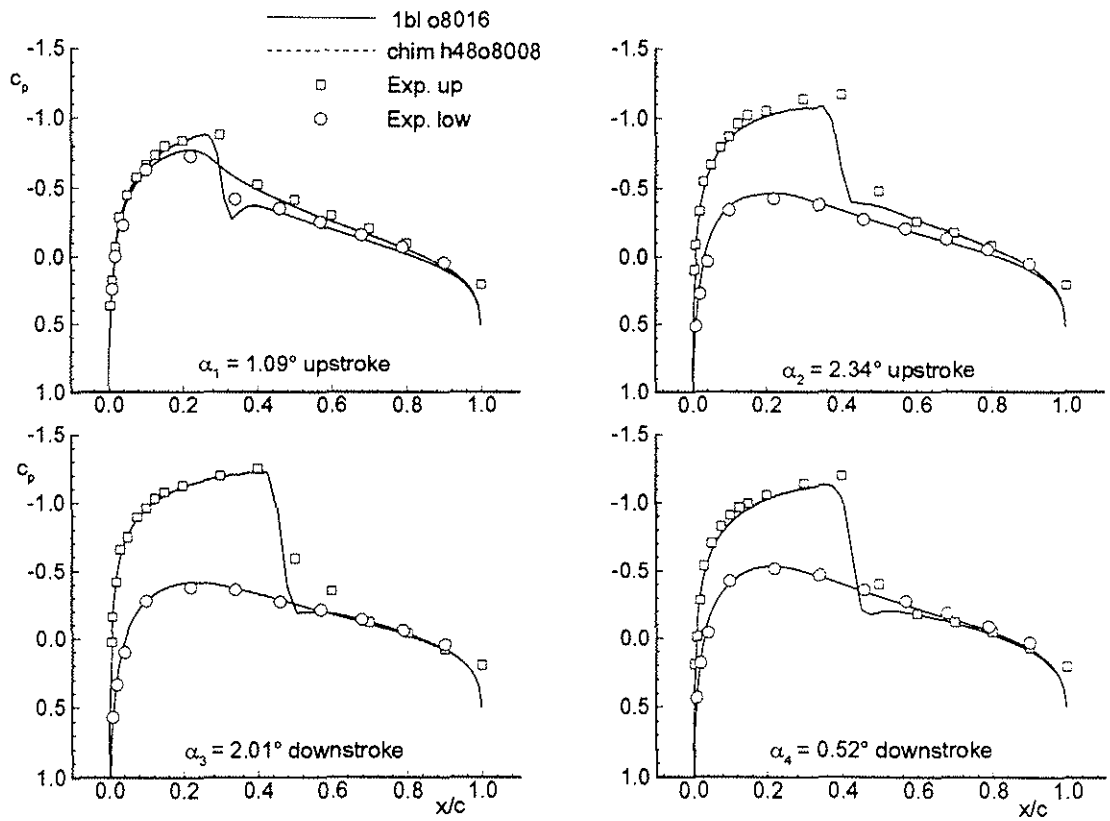

$$M_\infty = 0.755\,,\; k = 0.0814\,,\; \alpha = 0.016° + 2.51° \cdot \sin(\omega \cdot t)$$

Figure 7: Instantaneous Pressure Distributions for a NACA 0012 Airfoil Oscillating around its Quarter Point for the Coarse Grids

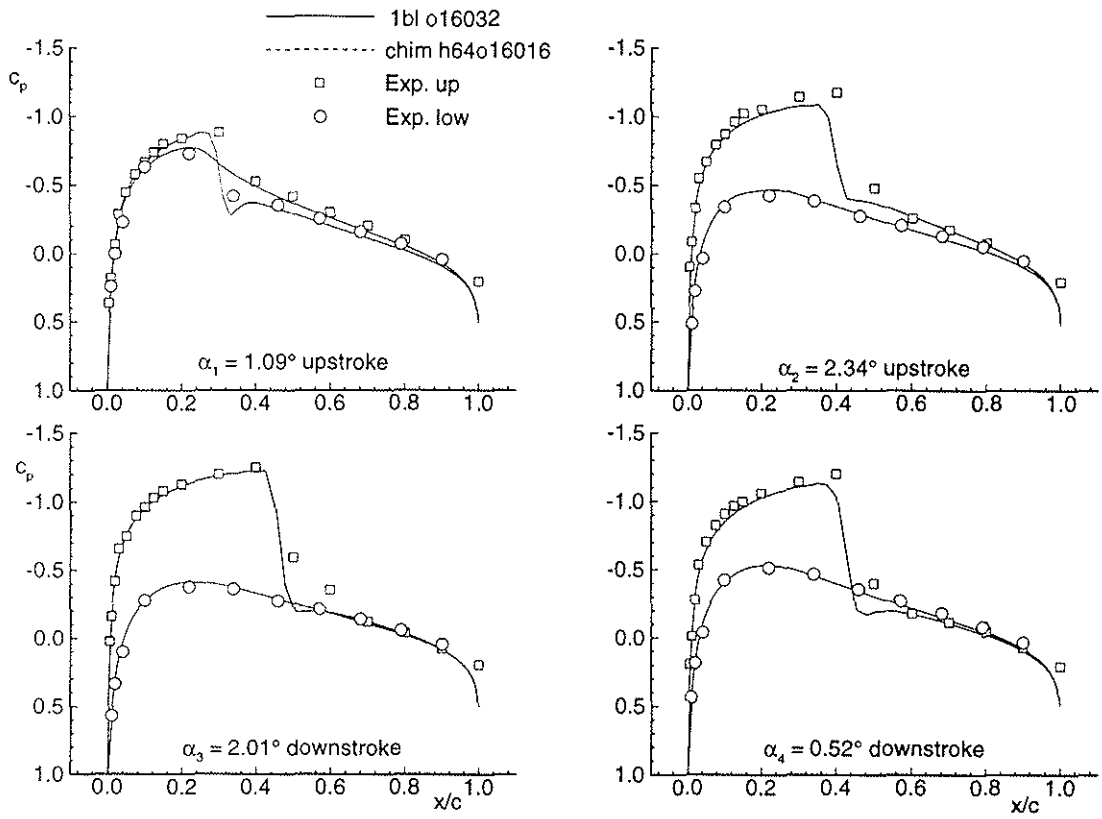

$$M_\infty = 0.755,\ k = 0.0814,\ \alpha = 0.016° + 2.51° \cdot \sin(\omega \cdot t)$$

Figure 8: Instantaneous Pressure Distributions for a NACA 0012 Airfoil Oscillating around its Quarter Point for the Medium Grids

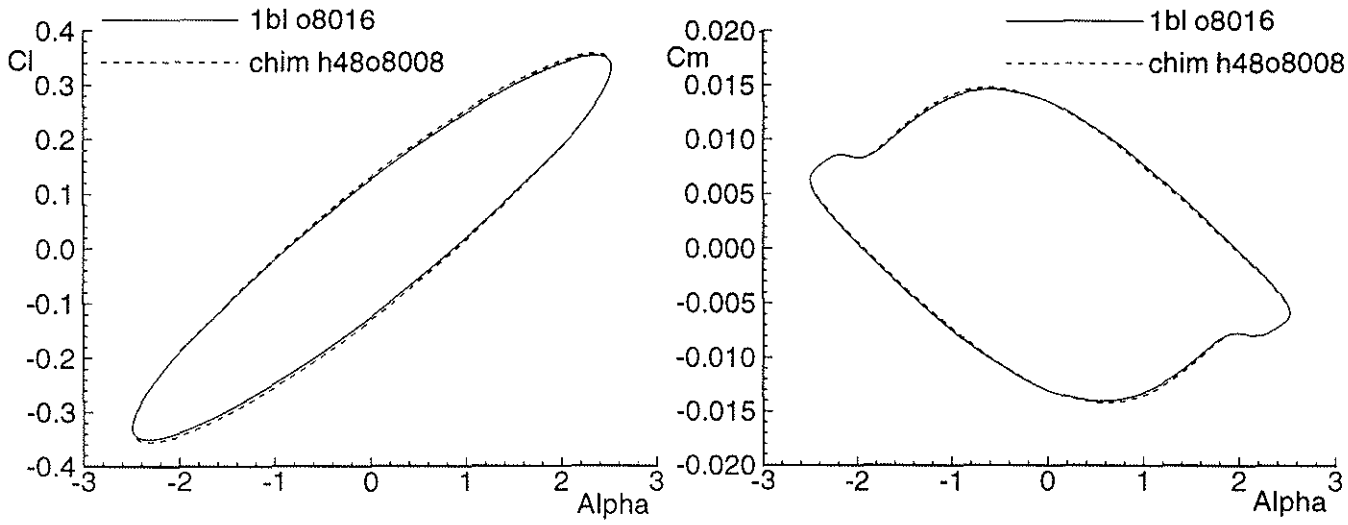

$$M_\infty = 0.755,\ k = 0.0814,\ \alpha = 0.016° + 2.51° \cdot \sin(\omega \cdot t)$$

Figure 9: Lift and Moment Coefficient for a NACA 0012 Airfoil Oscillating around its Quarter Point for the Coarse Grids

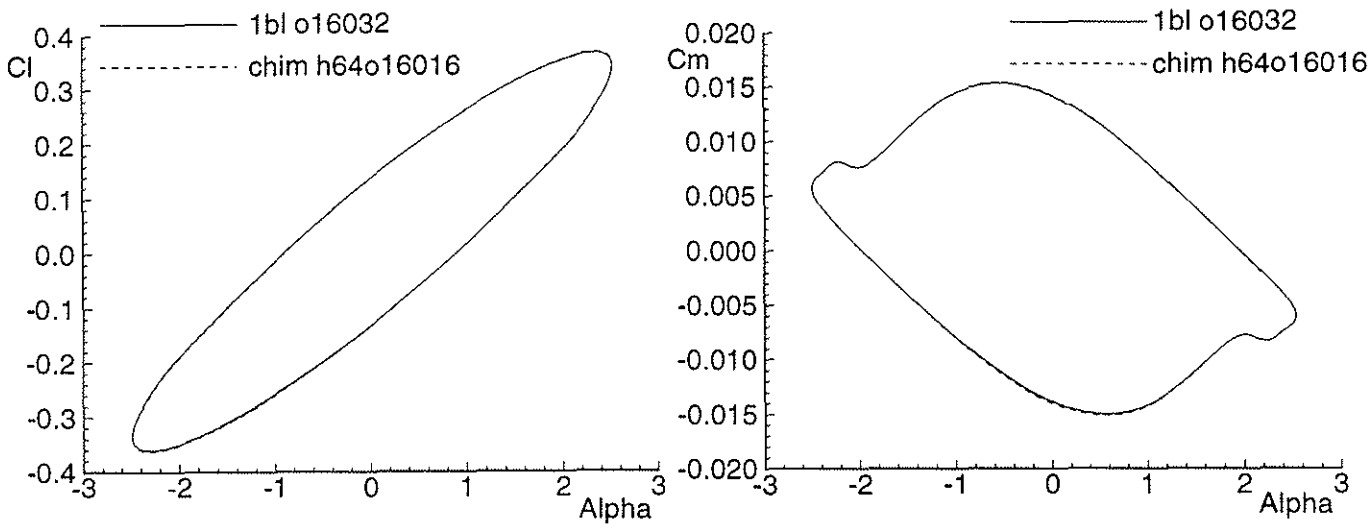

$$M_\infty = 0.755\,,\; k = 0.0814\,,\; \alpha = 0.016° + 2.51° \cdot \sin(\omega \cdot t)$$

Figure 10: Lift and Moment Coefficient for a NACA 0012 Airfoil Oscillating around its Quarter Point for the Medium Grids

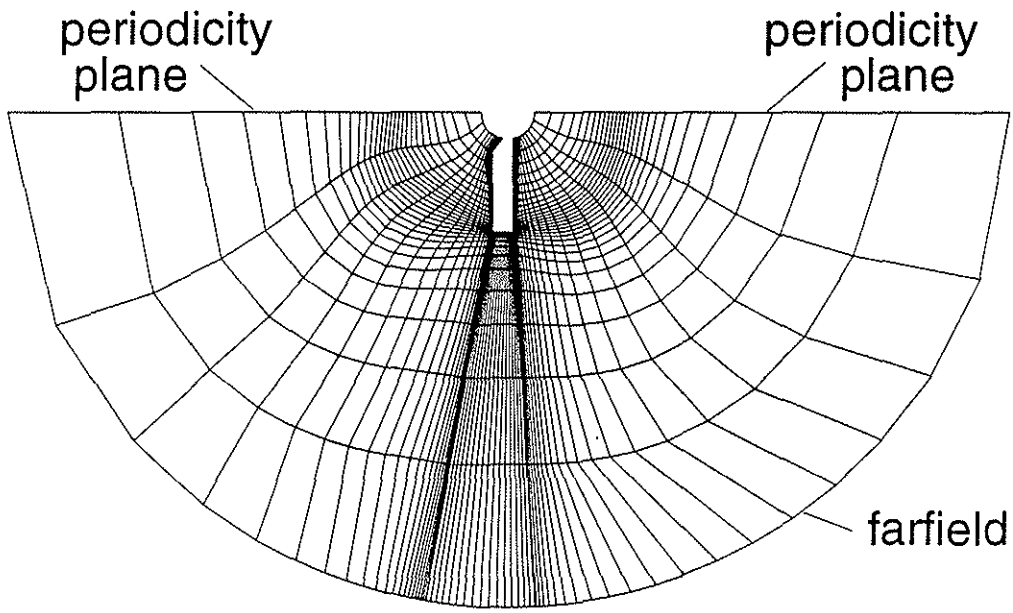

Figure 11: Grid in the Rotor Plane of a 2-Bladed Rotor

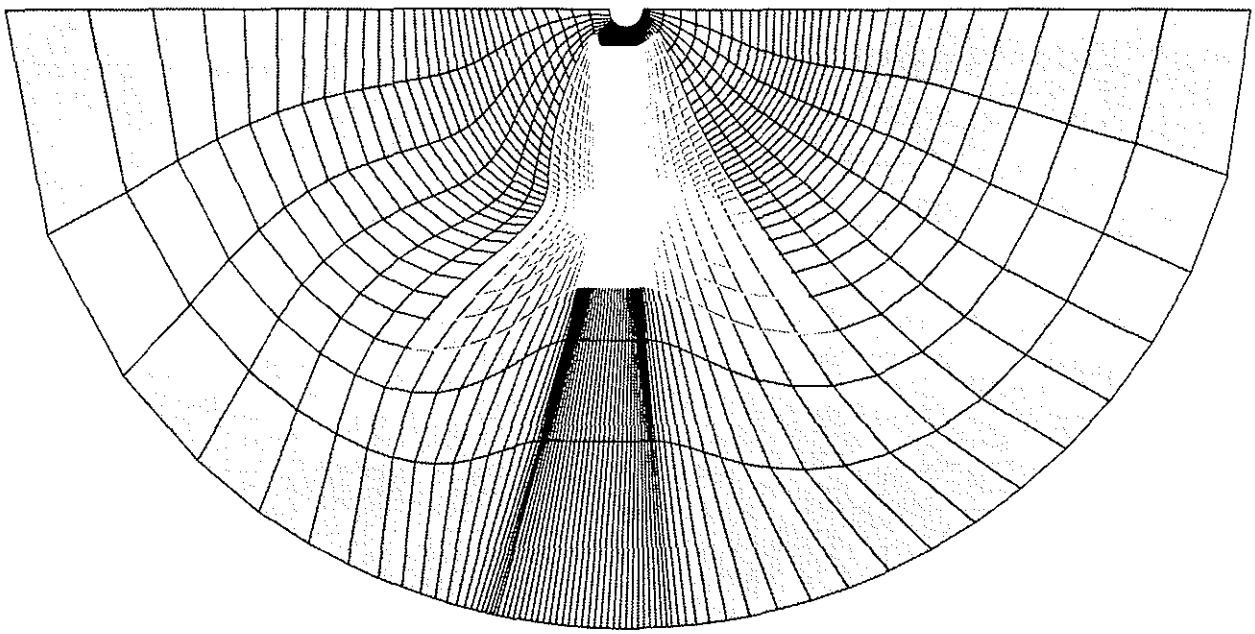

Figure 12: Grid of the Father (Black Lines) and the Child (White Lines) Grid in the Rotor Plane

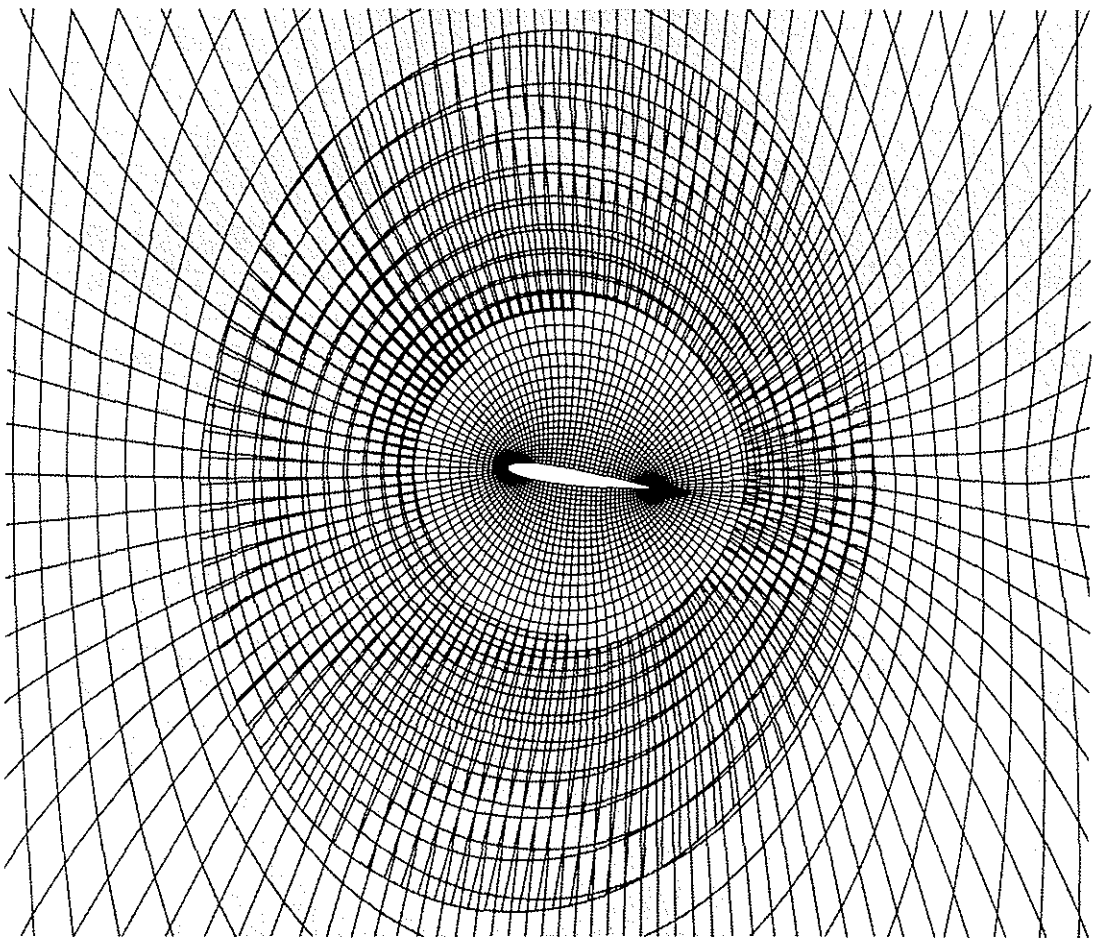

Figure 13: Father and Child Grid in a Cross Section at r/R=0.5
(Hole Cells not Shaded)

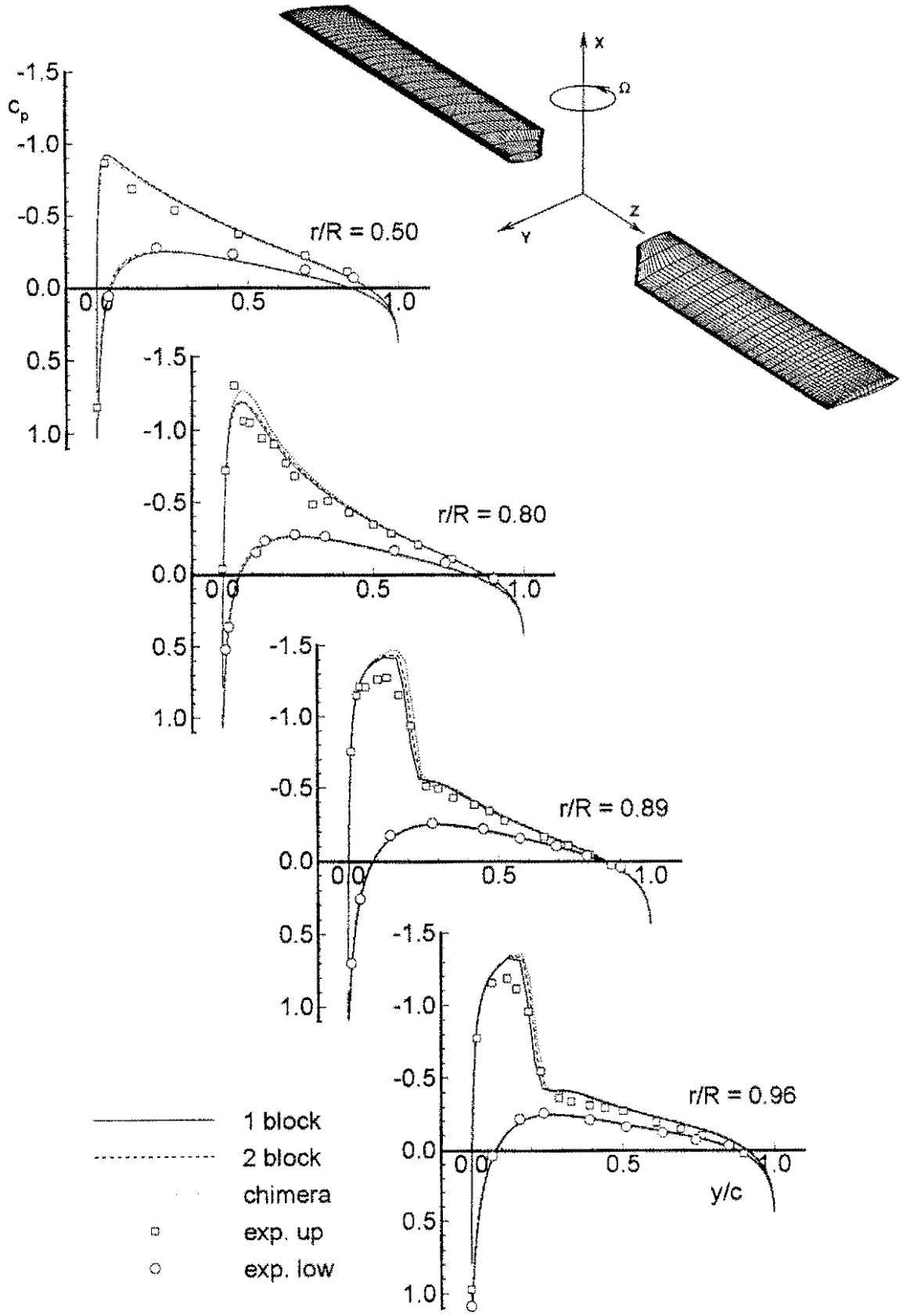

Figure 14: Surface Grid and Pressure Distributions of the 2-Blad. Caradonna-Tung Model Rotor ($M_{\omega R} = 0.794$, $\theta = 8°$)

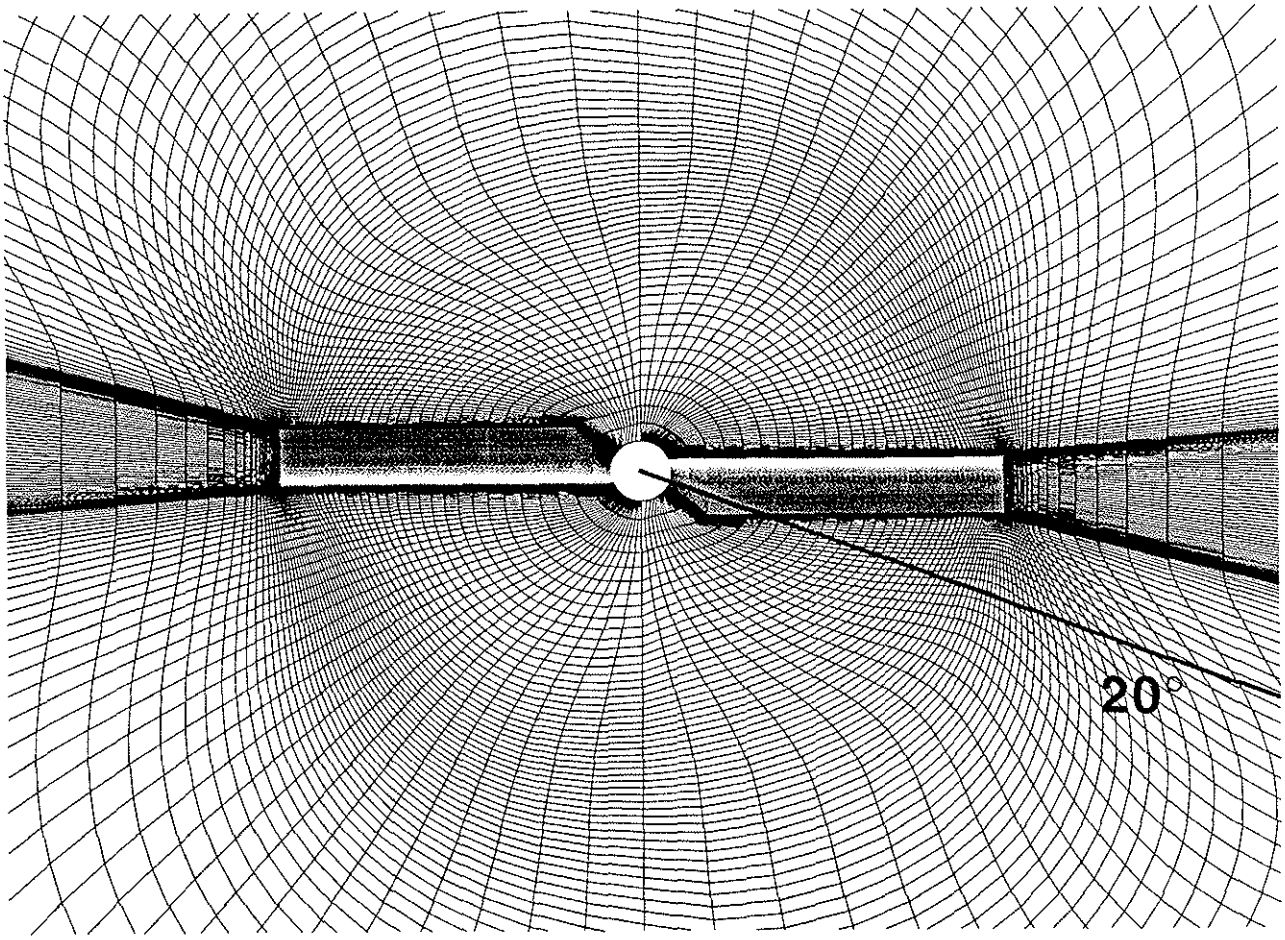

Figure 15: Azimuthal Position of the Plane for Vorticity Visualization of Figure 16

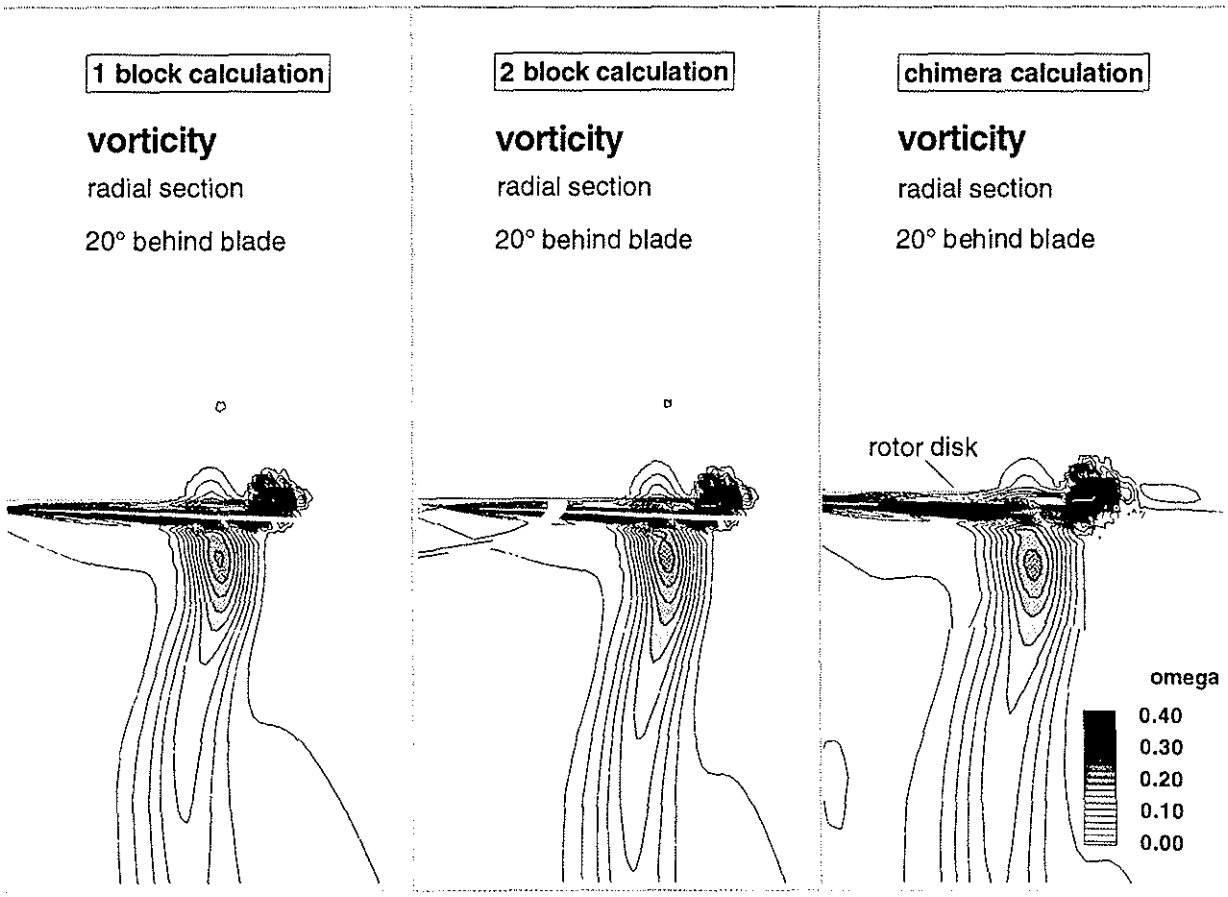

Figure 16: Vorticity Isolines for Caradonna-Tung Model Rotor in Hover
(20° Behind Rotor Blade, $M_{\omega R} = 0.794$, $\theta = 8°$)